

RESEARCH ARTICLE | SEPTEMBER 20 2023

# Tunable flatband plasmonic quasi-bound states in the continuum based on graphene-assisted metasurfaces

Special Collection: **Non-Hermitian Photonics**

Zhuo Wang ; Yue Wang ; Zhi Cheng; Jiaqi Qu; Mingjie Cui; Dongmei Huang ; Changyuan Yu  



*Appl. Phys. Lett.* 123, 121703 (2023)

<https://doi.org/10.1063/5.0166140>



## Articles You May Be Interested In

Fractal-like photonic lattices and localized states arising from singular and nonsingular flatbands

*APL Photonics* (November 2021)

High-quality flatband resonances in few-cell moiré superlattices by band-offset tuning

*Appl. Phys. Lett.* (May 2024)

Flatbands in frustrated lattice  $X_3\text{MnN}_3$  ( $X = \text{Ca}, \text{Sr}, \text{Ba}$ ): A first-principles study

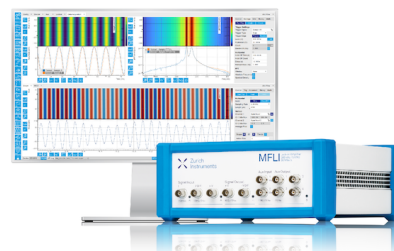
*J. Appl. Phys.* (July 2023)

## Challenge us.

What are your needs for periodic signal detection?



[Find out more](#)



# Tunable flatband plasmonic quasi-bound states in the continuum based on graphene-assisted metasurfaces

Cite as: Appl. Phys. Lett. **123**, 121703 (2023); doi: [10.1063/5.0166140](https://doi.org/10.1063/5.0166140)

Submitted: 3 July 2023 · Accepted: 27 August 2023 ·

Published Online: 20 September 2023



View Online



Export Citation



CrossMark

Zhuo Wang,<sup>1</sup> , Yue Wang,<sup>1</sup> , Zhi Cheng,<sup>1</sup> Jiaqi Qu,<sup>1</sup> Mingjie Cui,<sup>1</sup> Dongmei Huang,<sup>1</sup> , and Changyuan Yu<sup>1,2,a)</sup>

## AFFILIATIONS

<sup>1</sup>Photonics Research Institute, Department of Electrical and Electronic Engineering, The Hong Kong Polytechnic University, Kowloon, Hong Kong

<sup>2</sup>The Hong Kong Polytechnic University Shenzhen Research Institute, Shenzhen 518057, China

**Note:** This paper is part of the APL Special Collection on Non-Hermitian Photonics.

<sup>a)</sup>Author to whom correspondence should be addressed: [changyuan.yu@polyu.edu.hk](mailto:changyuan.yu@polyu.edu.hk)

## ABSTRACT

Bound states in the continuum (BICs) of plasmonic systems offer a powerful method for enhancing light-matter interaction at the nanoscale. The recent emergence of flatband quasi-BICs has alleviated the limitation of the incident angle of the excitation light on generating high-quality-factor (high-Q-factor) resonances, which makes it feasible to produce substantial near-field enhancement by focused light. However, the current works are limited to passive systems with fixed amplitude and Q-factor, hindering the dynamic tunability of light field enhancement. Here, we design a plasmonic metasurface integrated with monolayer graphene to achieve tunable flatband quasi-BICs. Under the illumination of a tightly focused transverse-magnetic wave, our simulations show that adjusting the chemical potential of graphene can increase Q-factor from 52.5 to 75.9 and improve absorption amplitude from 81% to 95%. These results pave the way for dynamically adjustable near-field enhancement with tightly focused light.

Published under an exclusive license by AIP Publishing. <https://doi.org/10.1063/5.0166140>

Bound states in the continuum (BICs) are nonradiative resonant modes overlapped with the spectrum of the radiation continuum. The concept of BICs was first proposed by von Neumann and Wigner in quantum models.<sup>1</sup> It is now considered to be a universal phenomenon in wave systems, including photonics,<sup>2</sup> plasmonics,<sup>3–5</sup> acoustics,<sup>6</sup> and optomechanics.<sup>7</sup> When an open system has structural symmetry, the constraints of symmetry can completely decouple resonant modes from all radiation channels. These bound states are classified as symmetry-protected (SP)-BICs.<sup>8</sup> BICs can still exist in systems where symmetry is missing.<sup>9</sup> A well-known example is Friedrich-Wintgen (FW)-BIC, which is formed by the interference of resonances belonging to different channels.<sup>10</sup> In addition, a pair of adjacent identical resonances can form BICs by canceling the radiation of each other.<sup>11</sup> The same mechanism can also be applied to a system consisting of a single resonance and its mirror image.<sup>12–14</sup> Theoretically, true BICs can achieve infinite quality-factors (Q-factors) in a boundary-free lossless model. In practice, due to geometric deformation, limited size, and other perturbations, BICs appear as quasi-BICs with finite high Q-factor. Quasi-BICs can be excited by optical beams from far field,

and the high-Q characteristic makes quasi-BICs important for generating sharp resonances and realizing ultrahigh near-field enhancement, which paves the way for miniaturized lasers,<sup>15–17</sup> ultrasensitive sensing,<sup>18,19</sup> and optical modulation.<sup>20–22</sup>

High-Q resonances governed by flatband quasi-BICs have attracted extensive attention in recent years. Ultralow dispersion in the momentum space makes this type of resonance have strong tolerance to light with low spatial coherence. Consequently, high-Q quasi-BICs can be excited by tightly focused light, which fundamentally improves the utilization efficiency of light energy for near-field enhancement. Specifically, a bionic plasmonic metasurface that was demonstrated can support surface lattice resonances (SLRs) with ultralow angular dispersion.<sup>23</sup> Under the joint effect of SP-BIC and FW-BIC, the SLRs stimulated by the transverse-magnetic (TM) polarized wave can maintain high Q-factors in the range of incident angles from 0° to 60°. Another work employed deep-subwavelength periodic structures to realize polarization insensitive flatband quasi-BICs.<sup>14</sup> It was found that high-Q (~71) resonances can be excited by focused light with a numerical aperture (NA) of 0.5. In addition, the energy-momentum

dispersion relation can be tuned by symmetry breaking.<sup>24</sup> Using band folding effects, flatband-edge quasi-BICs can be adjusted to off- $\Gamma$  points in the first Brillouin zone,<sup>25</sup> which can reduce the damage of angular dispersion on augmented reality (AR) images at large angle oblique incidence. However, in the above-mentioned passive systems, the Q-factor and resonant wavelength of the flatband quasi-BICs cannot be dynamically adjusted, which limits the scope of application.

The combination of two-dimensional (2D) materials and metasurfaces provides a solution for realizing active micro-nano devices.<sup>26</sup> For example, photonic metasurfaces can greatly enhance the second harmonic generation from few-layer GaSe<sup>27</sup> and transition metal dichalcogenides (TMDs)<sup>28</sup> by the BICs mechanism. In addition, utilizing the photoelectric properties of 2D materials, quasi-BICs become adjustable by varying the bias voltage.<sup>29,30</sup> However, the responses of those devices are sensitive to the wavevector direction of the incident light, rendering challenges for manipulating focused light.

Here, we proposed a plasmonic metasurface integrated with monolayer graphene to achieve tunable high-Q quasi-BICs for tightly focused TM polarized light. An ultralow average angular dispersion of  $-0.06 \text{ nm}/^\circ$  was found when the elevation angle ( $\theta$ ) of incidence varies from  $0^\circ$  to  $40^\circ$ . The Q-factor and resonant wavelength of quasi-BICs can be adjusted by changing the chemical potential ( $\mu_c$ ) of graphene. Significant Q-factor improvement (from  $\sim 52.5$  to  $\sim 75.9$ ) was found when  $\mu_c$  increased from 0 to 0.6 eV. The designed metasurface demonstrates dynamically adjustable flatband BICs, promising various potential applications, including nanolaser, nonlinear enhancement, and biosensing.

The geometry of the proposed metasurface is shown in Fig. 1(a). An array of nanoblocks with the same period  $P$  in  $x$  and  $y$  directions is placed on a silica ( $\text{SiO}_2$ ) spacer. The nanoblock consists of three pieces

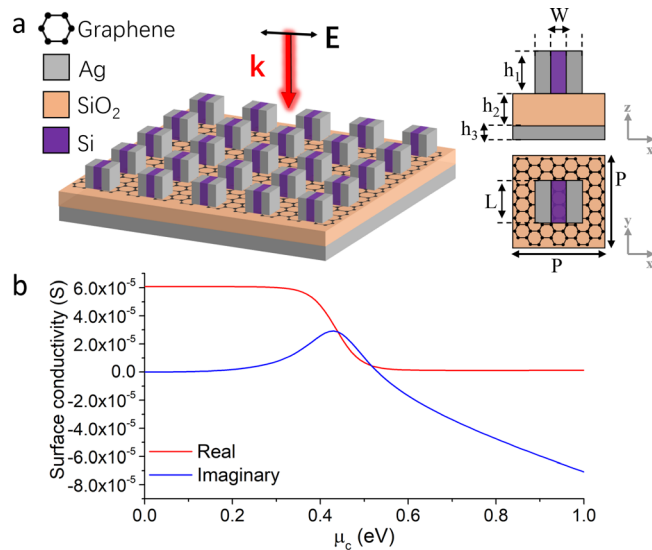


**FIG. 1.** Schematic of the graphene-assisted metasurface. (a) The metasurface consists of a bottom Ag layer, a middle  $\text{SiO}_2$  spacer, and a top nanoblock array. The monolayer graphene is placed between the spacer and nanoblock array. The front and top views of a unit cell are illustrated in the right-hand panel. (b) The real part and imaginary part of graphene surface conductivity vs chemical potential  $\mu_c$  at the wavelength of 1425 nm.

of elements; they are a middle silicon (Si) layer and two side silver (Ag) layers. The monolayer graphene is in the interface between nanoblocks and the spacer layer. The Ag layer at the bottom is mainly for generating specular reflection. The parameters for the design are as follows:  $P = 400 \text{ nm}$ ,  $W = 60 \text{ nm}$ ,  $L = 160 \text{ nm}$ ,  $h_1 = 160 \text{ nm}$ ,  $h_2 = 240 \text{ nm}$ , and  $h_3 = 100 \text{ nm}$ . The refractive indices of  $\text{SiO}_2$  and Si are modeled by the Sellmeier formula<sup>31</sup> and data obtained by Li,<sup>32</sup> respectively. The complex refractive index of Ag is obtained from the experimental results.<sup>33</sup>

The optical property of monolayer graphene can be described by the Kubo formula,<sup>34</sup>

$$\sigma_{\text{intra}} = \frac{-ie^2 k_B T}{\pi \hbar^2 (\omega - i2\Gamma)} \left[ \frac{\mu_c}{k_B T} + 2 \ln \left( \exp \left( \frac{-\mu_c}{k_B T} \right) + 1 \right) \right], \quad (1)$$

$$\sigma_{\text{inter}} = \frac{-ie^2 (\omega - i2\Gamma)}{\pi \hbar^2} \int_0^\infty \frac{f_d(-\xi) - f_d(\xi)}{(\omega - i2\Gamma)^2 - 4(\xi/\hbar)^2} d\xi, \quad (2)$$

where  $f_d(\xi) = (\exp((\xi - \mu_c)/k_B T) + 1)^{-1}$  is the Fermi-Dirac distribution,  $e$  is the elementary charge,  $k_B$  is Boltzmann's constant,  $\hbar$  is reduced Planck's constant, and  $\omega$  is the angular frequency of light. The total surface conductivity  $\sigma$  of graphene is the sum of the intra-band conductivity  $\sigma_{\text{intra}}$  and the inter-band conductivity  $\sigma_{\text{inter}}$ . At the near-infrared wavelength band, the real part of graphene surface conductivity  $\text{Re}(\sigma)$  is dominated by the inter-band transition, which affects the Q-factor of resonant modes. On the other hand, the imaginary part of graphene surface conductivity  $\text{Im}(\sigma)$  is determined by the combined effect of inter-band transition and intra-band transition. It will affect the wavelength of the resonant peak. In our simulation, the temperature is  $T = 300 \text{ K}$ , and the scattering parameter is  $\hbar\Gamma = 5 \text{ meV}$ .<sup>35,36</sup> As an example, at the wavelength of 1425 nm, the calculated real part and imaginary part of  $\sigma$  against  $\mu_c$  are shown in Fig. 1(b). When a bias voltage is applied between the graphene and the metal substrate,  $\mu_c$  can be changed,<sup>37</sup> so the metasurface is electrically adjustable.

In the metal-insulator-metal (MIM) nanoblock, the free current in the metal layers and the displacement current in the insulator can form a closed-loop current.<sup>38</sup> Hence, a magnetic dipole (MD) dominated resonance can be generated. Moreover, the interference between the MD and the light reflected by the Ag substrate can reduce the radiation toward the  $z$  direction, which significantly improves the Q-factor of resonance.<sup>13,14</sup> In the previous work, it was shown that MD-dominated BICs could be achieved by adjusting the height of the spacer layer.<sup>39</sup> Figure 2(a) (bottom panel) shows the magnetic field of resonance under the normal incidence of the TM polarized wave in the  $x$ - $y$  incident plane, and a strong MD polarized in the  $y$  direction can be found. When the incident angle  $\theta$  of the TM polarized wave changes [see the top panel of Fig. 2(a)], the magnetic polarization keeps in the  $y$  direction. Therefore, in a wide range of incident angles, the TM polarized wave can effectively excite the MD resonance.

We first used a full-wave solver based on finite element analysis software COMSOL Multiphysics to model the reflectance spectra of the metasurface under the excitation of the TM polarized wave at different incident angles. Because monolayer graphene is only a single atomic layer thick ( $\sim 0.34 \text{ nm}$ ), in the simulation it can be considered a 2D material with no thickness,<sup>40</sup> and its response to the light field can be described by the surface current density as  $J = \sigma E$ . Figures 2(b) and 2(c) show the results in the conditions of  $\mu_c = 0 \text{ eV}$  and

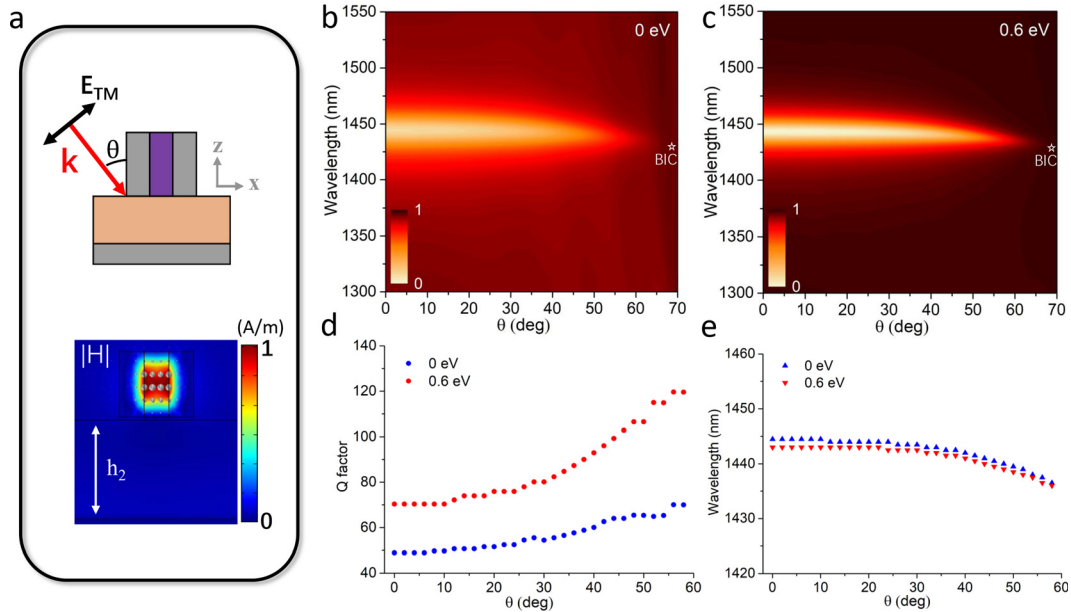


**FIG. 2.** TM excitation under different incident angles. (a) Schematic of oblique incidence of the TM polarized wave in the  $x$ - $z$  incident plane (top panel) and magnetic field distribution at the resonant wavelength (bottom panel). (b) and (c) Reflectance spectra vs incident angle  $\theta$  when the chemical potential is 0 and 0.6 eV, respectively. (d) Calculated Q-factors of resonances according to the reflection spectra. (e) Variation in the resonant wavelength with the incident angle.

$\mu_c = 0.6$  eV, respectively. At the incident angle around  $70^\circ$ , we can find an accidental BIC, of which the coupling with all radiation channels is inhibited. This accidental BIC can be classified as Fabry-Pérot (FP)-BICs,<sup>9</sup> and it is formed by the destructive interference between MD-dominated resonance with its mirror image.<sup>13</sup> When  $\theta$  decreases from the angle of BIC condition, the BIC evolves into quasi-BICs with the increase in the spectral linewidth and resonant depth. For both cases of  $\mu_c = 0$  eV and  $\mu_c = 0.6$  eV, the angular dispersion of the quasi-BICs is very weak, and especially in the range from  $0^\circ$  to  $40^\circ$  of  $\theta$ , the quasi-BICs can maintain a very small resonant wavelength offset ( $<3$  nm) and a large absorption amplitude ( $>65\%$ ). The Q-factors of the excited resonances can be calculated by the formula  $Q = \omega_r / \Delta\omega$ , where  $\omega_r$  is the resonant angular frequency and  $\Delta\omega$  is the full width of half maximum (FWHM) of the reflectance spectrum. Figure 2(d) shows the Q-factors of quasi-BICs vs  $\theta$  under two different graphene chemical potentials. As the incident angle approaches the BIC condition, the Q-factors can be significantly increased due to the reduction of radiative loss. In addition, when  $\mu_c$  increases from 0 to 0.6 eV, the Q-factors of quasi-BICs are effectively boosted by at least 20. From the results in Fig. 1(b), we can find that the real part of  $\sigma$  drops from  $6.09 \times 10^{-5}$  S to almost 0 S when  $\mu_c$  grows from 0 to 0.6 eV; consequently, the dissipative loss of graphene is reduced, and the Q-factors of quasi-BICs are improved. Therefore, in the proposed metasurface, the Q-factors of quasi-BICs can be tuned by adjusting the radiative loss and dissipative loss at the same time. Another merit of the design is that the weak angular dispersion characteristic of quasi-BICs is not influenced by the change in the graphene surface conductivity. According to the results in Fig. 2(e), changing  $\mu_c$  just leads to a small shift of resonant wavelength, while the property of weak angular dispersion keeps well.

The weak angular dispersion of the metasurface originates from the intrinsic flatband characteristic of the deep sub-wavelength periodic structure. We used the eigenfrequency solver of COMSOL Multiphysics to analyze the band structure of the metasurface. In the simulation, the Floquet periodic boundary condition was adopted in the transverse boundaries. The wave vector for Floquet periodicity in the  $x$  and  $y$  directions are  $k_x$  and  $k_y$ , respectively. To match the condition that the incident plane is  $x$ - $z$  plane,  $k_y$  keeps to be zero, and  $k_x$  varies from 0 to  $0.54\pi/P$ . The calculated band structures with different  $\mu_c$  are shown in Fig. 3(a). It can be seen that in all cases, the eigenwavelength just decreases by about 2.4 nm when  $k_x$  increases from 0 to  $0.36\pi/P$ . The correspondence between  $\theta$  and  $k_x$  is given by  $\theta = \arcsin(k_x/k_r)$ , where  $k_r$  is the free-space wave vector at the resonant wavelength. It can be obtained that  $\theta$  is around  $40^\circ$  when  $k_x = 0.36\pi/P$ . Therefore, the angular dispersion is very low with a value of  $-0.06$  nm/ $^\circ$ . In addition, the resonant wavelength is affected by  $\text{Im}(\sigma)$ . When  $\mu_c$  grows from 0 to 0.4 eV, the resonant wavelength has a redshift of about 2 nm. After that, continuing to increase  $\mu_c$  to 0.5 and 0.6 eV will cause a blueshift in the resonant wavelength. These results are consistent with the variation trend of  $\text{Im}(\sigma)$  in Fig. 1(b), which increases first and then decreases. The Q-factor of eigenmodes can be defined by  $Q = \text{Re}(\omega_e) / \text{Im}(2\omega_e)$ , where  $\text{Re}(\omega_e)$  and  $\text{Im}(\omega_e)$  are the real and imaginary parts of the eigen angular frequency, respectively. Figure 3(b) illustrates that the Q-factors grow with the increase in  $k_x$ . They reach the maximum around  $k_x = 0.53\pi/P$ , the equivalent incident angle of which is about  $70^\circ$ . The trend agrees well with the data obtained from the reflectance spectra. In addition, the Q-factors of eigenmodes increase steadily as  $\mu_c$  grows step by step from 0 to 0.6 eV. The reason is that the increase in  $\mu_c$  reduces the graphene dissipative loss caused by  $\text{Re}(\sigma)$ . The maximum average improvement of

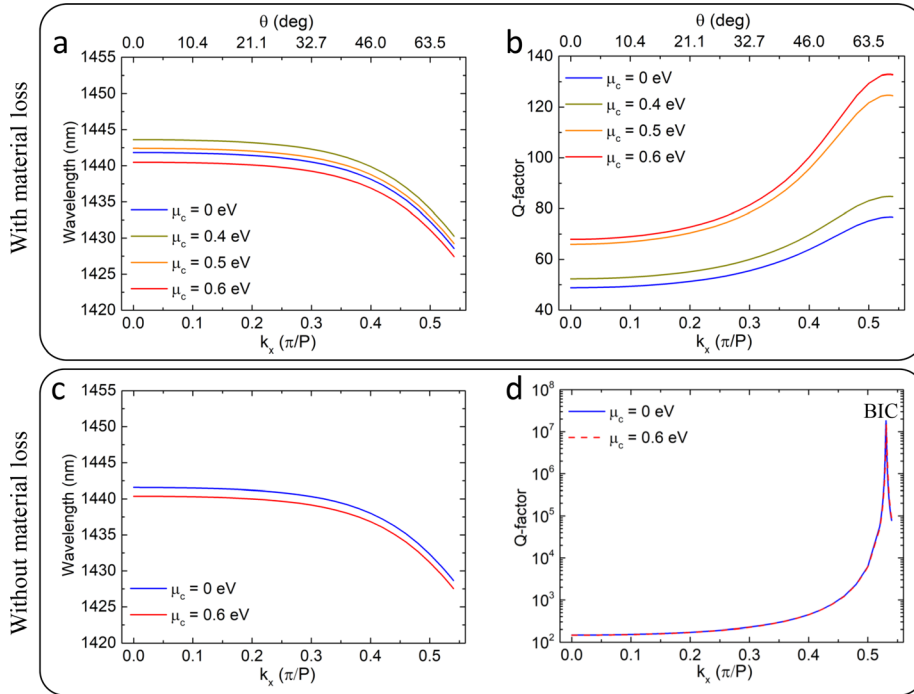


**FIG. 3.** Eigenmode analysis of metasurface. (a) and (b) Resonant wavelength and Q-factor of eigenmodes vs  $x$ -direction wave vector  $k_x$  and the corresponding incident angle  $\theta$  of TM polarized wave, respectively. (c) and (d) The results of resonant wavelength and Q-factor, respectively, in the case of ignoring all material loss.

the Q-factors is about 23 when  $k_x$  is in the range of  $[0, 0.36 \pi/P]$ . Therefore, the robustness of the high Q-factor and flatband structure makes the metasurface capable to generate tunable high-Q resonances under focused light illumination.

The presence of FP-BIC at oblique incidence can be further demonstrated in the case of eliminating material loss. The imaginary part of the relative permittivity  $\text{Im}(\epsilon_r)$  of Ag is ignored, so Ag is regarded as a perfect conductor. The real part of the surface conductivity of graphene  $\text{Re}(\sigma)$  is set to be zero. In addition, the refractive indexes of all dielectric materials are real. The results are shown in the lower panel of Fig. 3. The eigenwavelengths in Fig. 3(c) agree well with the results in Fig. 3(a), which indicates that the material loss has little influence on the resonant wavelength. In Fig. 3(d), because  $\text{Re}(\sigma) \equiv 0$ , the change of  $\mu_c$  does not affect the Q-factor. We can see that the Q-factors of eigenmodes approach infinity when  $k_x$  is about  $0.53 \pi/P$ . The corresponding incident angle is around  $70^\circ$ . This result is consistent with the angle at which the resonant peak disappears in Fig. 2, which provides solid evidence for the existence of BIC.

Next, we analyze the resonances under transverse-electric (TE) polarized wave incidence. As illustrated in Fig. 4(a), the magnetic component of incidence is in the  $x$ - $z$  plane. The  $z$ -component of magnetic field will increase with  $\theta$ ; hence, a  $z$ -direction magnetic dipole can be stimulated by oblique incidence. The reflectance spectra when  $\mu_c = 0.6$  eV are shown in Fig. 4(b). Since the normal incidence cannot excite the  $z$ -direction magnetic dipole, no resonant dip appears. With the increase in  $\theta$ , the resonance depth first increases and then decreases, and the perfect absorption is reached at about  $30^\circ$ . At the same time, the linewidth of the resonance continues to broaden. This is a typical phenomenon of the evolution from BIC to quasi-BIC. Then we calculated the Q-factors of eigenmodes without material loss

as shown in Fig. 4(e). The Q-factor approaches infinity when  $k_x = 0$ , which confirms the existence of SP-BIC. The results of eigenwavelength are shown in Fig. 4(c). The increase in  $\mu_c$  from 0 to 0.6 eV also causes a blueshift. The decrease in the resonant wavelength is about 12 nm when  $k_x$  increases from 0 to  $0.36 \pi/P$ . Thus, the corresponding angular dispersion is about  $-0.3 \text{ nm}/^\circ$ , which is five times larger than that of the TM incidence. Then, the Q-factors of eigenmodes with material loss are illustrated in Fig. 4(d). When  $k_x$  is in the range from 0 to  $0.2 \pi/P$ , the Q-factor can be significantly improved by increasing  $\mu_c$  from 0 to 0.6 eV. However, when  $k_x$  approaches  $0.5 \pi/P$ , the radiative loss dominates. Consequently, the increase in  $\mu_c$  can only slightly increase the Q-factor.

By comparing the results of TM incidence and TE incidence, the TM incidence has the advantages of vertical excitation and ultraweak angular dispersion, which is more suitable for field enhancement of focused light. To mimic the condition of focused illumination, we calculated the average reflectance spectra ( $\bar{R}$ ) of the TM polarized wave in the  $x$ - $z$  incident plane covering the  $\theta$  from  $0^\circ$  to  $40^\circ$ . The expression is

$$\bar{R}(\lambda) = \frac{1}{N} \sum_{\theta=0^\circ}^{40^\circ} R_\theta^{\text{TM}}(\lambda), \quad (3)$$

where  $R_\theta^{\text{TM}}$  is the reflectance spectrum excited by the TM polarized wave at the incident angle  $\theta$ .  $N$  is the number of sampled  $\theta$ . Here,  $\theta$  changes from  $0^\circ$  to  $40^\circ$  in steps of  $2^\circ$ , as illustrated schematically by the inset of Fig. 5. Because the real part of graphene surface conductivity can cause dissipative loss, the maximum average reflectance is just  $\sim 0.9$  when  $\mu_c = 0$  eV. In this case, the Q-factor is relatively low at  $\sim 52.5$ , and the absorption amplitude is just  $\sim 81\%$ . With the increase



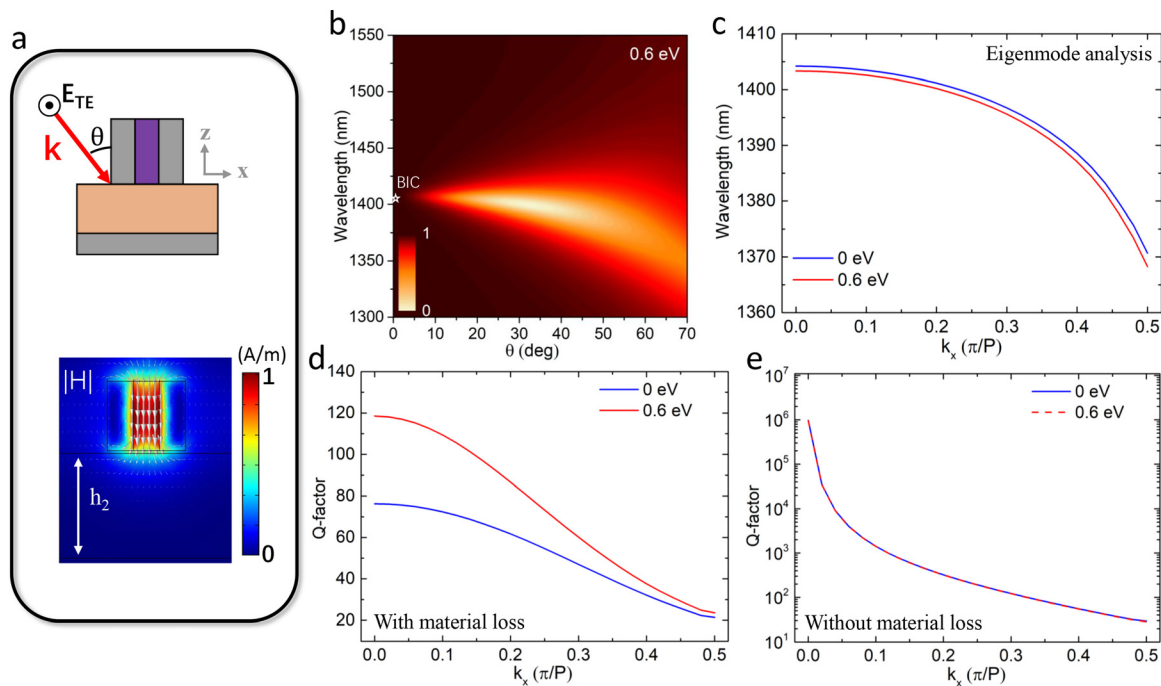


**FIG. 4.** TE excitation under different incident angles. (a) Schematic of oblique incidence of the TE wave in the  $x$ - $z$  incident plane (top panel) and magnetic field distribution at the resonant wavelength (bottom panel). (b) Reflectance spectra vs incident angle  $\theta$  when the chemical potential is 0.6 eV. (c) Resonant wavelength of eigenmodes vs  $x$ -direction wavenumber  $k_x$ . (d) and (e) The Q-factors of eigenmodes in the cases with and without material loss, respectively.

in  $\mu_c$ , the dissipation caused by  $\sigma$  decreases; hence, the Q-factor increases slightly to 56.6 at  $\mu_c = 0.4$  eV. When  $\mu_c$  is increased to 0.6 eV, the real part of  $\sigma$  becomes close to zero. At this time, the dissipative loss caused by graphene is minimized. Consequently, the Q-factor of the average reflectance spectra increases to  $\sim 75.9$ . In the meantime, the absorption amplitude grows to  $\sim 95\%$ . The further increase in  $\mu_c$  from 0.6 to 1 eV has little influence on the real part of  $\sigma$ . Instead, the imaginary part of  $\sigma$  is significantly decreased. Therefore, the resonant wavelength decreases by  $\sim 4$  nm, while the Q-factor and resonant depth almost do not change. Conventionally, the graphene

chemical potential does not exceed 1 eV. The resonant dips of  $\mu_c = 0.4$  and 1 eV are at 1438.5 and 1445.5 nm, respectively. Hence, the controllable spectrum range of flatband quasi-BICs is about 7 nm. The simulation results demonstrate that the designed metasurface can realize dynamically adjustable high-Q flatband quasi-BICs. It provides a way to regulate the interaction between matter and tightly focused light.

The TM polarized focused light of the  $x$ - $z$  incident plane mentioned above can be generated experimentally.<sup>23</sup> To reduce the undesired spatial components of incidence, the objective needs to be partially blocked by opaque tapes to form a slit along the  $x$ -direction as shown in the right panel of Fig. 5. The polarization of the focused light can be controlled by tuning the polarization of the collimated light incident to the objective. For example, the  $x$ -polarized collimated light passing through the modified objective will form a focused TM light. This method enables further experimental testing of the designed metasurface.

The proposed metasurface can be fabricated by a standard clean-room process, including electron beam lithography (EBL), electron beam deposition, and inductively coupled plasma (ICP) etching. A pioneer work has reported the fabrication of a vertically oriented MIM structure with a 25 nm channel sandwiched between two metal films,<sup>41</sup> and their processes support the fabrication feasibility of the structures we designed. The fabrication and measurement of the designed metasurface will be carried out in the future.

In this work, we proposed a plasmonic metasurface that can achieve tunable flatband quasi-BICs by changing the chemical potential of graphene. For the incidence of the TM polarized wave, the excited quasi-BICs have ultra-low average angular dispersion

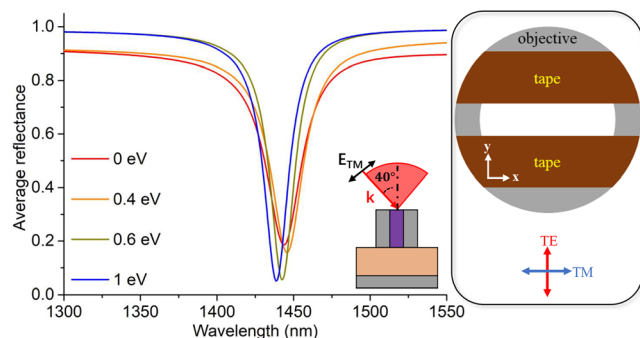


**FIG. 5.** Average reflectance spectra at different chemical potentials. The inset represents focused TM polarized waves with  $\theta$  covers from  $0^\circ$  to  $40^\circ$  in the  $x$ - $z$  incident plane illuminate on the metasurface. The right panel illustrates the method of generating the incident light by a partially blocked objective.

( $-0.06 \text{ nm}^2$ ) in the range of incident angles from  $0^\circ$  to  $40^\circ$ . Furthermore, due to the effect of FP-BICs, the high-Q characteristic of the resonance can be further enhanced at oblique incidence. Thus, the light-matter interaction will be improved by tightly focused TM polarized light based on the designed metasurface. More importantly, the flatband property of quasi-BICs is robust during tuning the surface conductivity of graphene. Instead, the Q-factor is adjustable by changing the dissipative loss of graphene. Consequently, under the illumination of focused TM polarized light with a high NA of  $\sim 0.64$ , the Q-factor of the stimulated resonance can be improved from  $\sim 52.5$  to  $\sim 75.9$  by increasing  $\mu_c$  from 0 to over 0.6 eV. Meanwhile, the absorption amplitude grows from  $\sim 81\%$  to  $\sim 95\%$ . This work opens up a way to achieve adjustable flatband quasi-BICs by combining deep sub-wavelength metasurfaces with 2D materials, which can be used in the fields of nanolaser, nonlinear enhancement, and biosensing.

The authors gratefully thank Dr. Yao Liang for fruitful discussions. This work was supported by the Hong Kong Research Grants Council (GRF Project No. 15209321), by the Innovation and Technology Fund (No. ITS/107/21FP), and by the Key Basic Research Scheme of the Shenzhen Natural Science Foundation (No. JCYJ20200109142010888).

## AUTHOR DECLARATIONS

### Conflict of Interest

The authors have no conflicts to disclose.

### Author Contributions

**Zhuo Wang:** Conceptualization (equal); Investigation (equal); Methodology (equal); Writing – original draft (equal). **Yue Wang:** Data curation (equal); Methodology (equal); Writing – review & editing (equal). **Zhi Cheng:** Investigation (equal); Methodology (equal). **Jiaqi Qu:** Investigation (equal); Methodology (equal). **Mingjie Cui:** Investigation (equal); Writing – review & editing (equal). **Dongmei Huang:** Funding acquisition (equal); Supervision (equal). **Changyuan Yu:** Conceptualization (equal); Funding acquisition (equal); Supervision (lead).

### DATA AVAILABILITY

The data that support the findings of this study are available from the corresponding author upon reasonable request.

## REFERENCES

1. J. von Neumann and E. P. Wigner, "Über das Verhalten von Eigenwerten bei adiabatischen Prozessen," *the Collected Works of Eugene Paul Wigner: Part A: The Scientific Papers* (Springer, 1993), pp. 294–297.
2. D. C. Marinica, A. G. Borisov, and S. V. Shabanov, "Bound states in the continuum in photonics," *Phys. Rev. Lett.* **100**, 183902 (2008).
3. Y. Liang, K. Koshelev, F. Zhang, H. Lin, S. Lin, J. Wu, B. Jia, and Y. Kivshar, "Bound states in the continuum in anisotropic plasmonic metasurfaces," *Nano Lett.* **20**, 6351–6356 (2020).
4. A. Aigner, A. Tittl, J. Wang, T. Weber, Y. Kivshar, S. A. Maier, and H. Ren, "Plasmonic bound states in the continuum to tailor light-matter coupling," *Sci. Adv.* **8**, eadd4816 (2022).
5. Y. Tang, Y. Liang, J. Yao, M. K. Chen, S. Lin, Z. Wang, J. Zhang, X. G. Huang, C. Yu, and D. P. Tsai, "Chiral bound states in the continuum in plasmonic metasurfaces," *Laser Photonics Rev.* **17**, 2200597 (2023).
6. I. Deriy, I. Toftul, M. Petrov, and A. Bogdanov, "Bound states in the continuum in compact acoustic resonators," *Phys. Rev. Lett.* **128**, 084301 (2022).
7. Y. Yu, X. Xi, and X. Sun, "Observation of mechanical bound states in the continuum in an optomechanical microresonator," *Light: Sci. Applicat.* **11**, 328 (2022).
8. K. Koshelev, S. Lepeshov, M. Liu, A. Bogdanov, and Y. Kivshar, "Asymmetric metasurfaces with high-q resonances governed by bound states in the continuum," *Phys. Rev. Lett.* **121**, 193903 (2018).
9. C. W. Hsu, B. Zhen, A. D. Stone, J. D. Joannopoulos, and M. Soljačić, "Bound states in the continuum," *Nat. Rev. Mater.* **1**, 1–13 (2016).
10. H. Friedrich and D. Wintgen, "Interfering resonances and bound states in the continuum," *Phys. Rev. A* **32**, 3231–3242 (1985).
11. W. Suh, M. F. Yanik, O. Solgaard, and S. Fan, "Displacement-sensitive photonic crystal structures based on guided resonance in photonic crystal slabs," *Appl. Phys. Lett.* **82**, 1999–2001 (2003).
12. C. W. Hsu, B. Zhen, S.-L. Chua, S. G. Johnson, J. D. Joannopoulos, and M. Soljačić, "Bloch surface eigenstates within the radiation continuum," *Light: Sci. Applicat.* **2**, e84 (2013).
13. G. Yang, S. U. Dev, M. S. Allen, J. W. Allen, and H. Harutyunyan, "Optical bound states in the continuum enabled by magnetic resonances coupled to a mirror," *Nano Lett.* **22**, 2001–2008 (2022).
14. Z. Wang, Y. Liang, J. Qu, M. K. Chen, M. Cui, Z. Cheng, J. Zhang, J. Yao, S. Chen, D. P. Tsai, and C. Yu, "Plasmonic bound states in the continuum for unpolarized weak spatially coherent light," *Photonics Res.* **11**, 260–269 (2023).
15. A. Kodigala, T. Lepetit, Q. Gu, B. Bahari, Y. Fainman, and B. Kanté, "Lasing action from photonic bound states in continuum," *Nature* **541**, 196–199 (2017).
16. X. Zhang, Y. Liu, J. Han, Y. Kivshar, and Q. Song, "Chiral emission from resonant metasurfaces," *Science* **377**, 1215–1218 (2022).
17. H. Zhong, Y. Yu, Z. Zheng, Z. Ding, X. Zhao, J. Yang, Y. Wei, Y. Chen, and S. Yu, "Ultra-low threshold continuous-wave quantum dot mini-BIC lasers," *Light: Sci. Applicat.* **12**, 100 (2023).
18. W. Suh, O. Solgaard, and S. Fan, "Displacement sensing using evanescent tunneling between guided resonances in photonic crystal slabs," *J. Appl. Phys.* **98**, 033102 (2005).
19. S. Romano, G. Zito, S. Torino, G. Calafiore, E. Penzo, G. Coppola, S. Cabrini, I. Rendina, and V. Mocella, "Label-free sensing of ultralow-weight molecules with all-dielectric metasurfaces supporting bound states in the continuum," *Photonics Res.* **6**, 726–733 (2018).
20. Z. Yu and X. Sun, "Acousto-optic modulation of photonic bound state in the continuum," *Light: Sci. Applicat.* **9**(1), 1 (2020).
21. M. M. Salary and H. Mosallaei, "Tunable all-dielectric metasurfaces for phase-only modulation of transmitted light based on quasi-bound states in the continuum," *ACS Photonics* **7**, 1813–1829 (2020).
22. X. Sun, J. Sun, Z. Wang, L. Wang, F. Qiu, and L. Wen, "Manipulating dual bound states in the continuum for efficient spatial light modulator," *Nano Lett.* **22**, 9982 (2022).
23. Y. Liang, H. Lin, S. Lin, J. Wu, W. Li, F. Meng, Y. Yang, X. Huang, B. Jia, and Y. Kivshar, "Hybrid anisotropic plasmonic metasurfaces with multiple resonances of focused light beams," *Nano Lett.* **21**, 8917–8923 (2021).
24. H. S. Nguyen, F. Dubois, T. Deschamps, S. Cuffe, A. Pardon, J.-L. Leclercq, C. Seassal, X. Letartre, and P. Viktorovitch, "Symmetry breaking in photonic crystals: On-demand dispersion from flatband to Dirac cones," *Phys. Rev. Lett.* **120**, 066102 (2018).
25. A. C. Overvig, M. Cotrufo, M. Markowitz, Y. Zhou, B. Hao, K. Stensvad, C. Schardt, and A. Alù, "Zone-folded quasi-bound state metasurfaces with customized, symmetry-protected energy-momentum relations," *ACS Photonics* **10**, 1832 (2023).
26. A. Elbanna, H. Jiang, Q. Fu, J.-F. Zhu, Y. Liu, M. Zhao, D. Liu, S. Lai, X. W. Chua, J. Pan, Z. X. Shen, L. Wu, Z. Liu, C.-W. Qiu, and J. Teng, "2D material infrared photonics and plasmonics," *ACS Nano* **17**, 4134–4179 (2023).
27. Z. Liu, J. Wang, B. Chen, Y. Wei, W. Liu, and J. Liu, "Giant enhancement of continuous wave second harmonic generation from few-layer GaSe coupled to high-Q quasi bound states in the continuum," *Nano Lett.* **21**, 7405–7410 (2021).

- <sup>28</sup>P. Hong, L. Xu, and M. Rahmani, "Dual bound states in the continuum enhanced second harmonic generation with transition metal dichalcogenides monolayer," *Opto-Electron Adv.* **5**, 200097 (2022).
- <sup>29</sup>C. Zhao, W. Chen, J. Wei, W. Deng, Y. Yan, Y. Zhang, and C.-W. Qiu, "Electrically tunable and robust bound states in the continuum enabled by 2D transition metal dichalcogenide," *Adv. Opt. Mater.* **10**, 2201634 (2022).
- <sup>30</sup>S. Xiao, X. Wang, J. Duan, T. Liu, and T. Yu, "Engineering light absorption at critical coupling via bound states in the continuum," *J. Opt. Soc. Am. B* **38**, 1325–1330 (2021).
- <sup>31</sup>I. H. Malitson, "Interspecimen comparison of the refractive index of fused silica," *J. Opt. Soc. Am.* **55**, 1205–1209 (1965).
- <sup>32</sup>H. H. Li, "Refractive index of silicon and germanium and its wavelength and temperature derivatives," *J. Phys. Chem. Reference Data* **9**, 561–658 (1980).
- <sup>33</sup>P. B. Johnson and R. W. Christy, "Optical constants of the noble metals," *Phys. Rev. B* **6**, 4370–4379 (1972).
- <sup>34</sup>G. W. Hanson, "Dyadic Green's functions and guided surface waves for a surface conductivity model of graphene," *J. Appl. Phys.* **103**, 064302 (2008).
- <sup>35</sup>A. B. Kuzmenko, E. van Heumen, F. Carbone, and D. van der Marel, "Universal optical conductance of graphite," *Phys. Rev. Lett.* **100**, 117401 (2008).
- <sup>36</sup>F. Xu, S. Das, Y. Gong, Q. Liu, H.-C. Chien, H.-Y. Chiu, J. Wu, and R. Hui, "Complex refractive index tunability of graphene at 1550 nm wavelength," *Appl. Phys. Lett.* **106**, 031109 (2015).
- <sup>37</sup>Y. Yao, R. Shankar, M. A. Kats, Y. Song, J. Kong, M. Loncar, and F. Capasso, "Electrically tunable metasurface perfect absorbers for ultrathin mid-infrared optical modulators," *Nano Lett.* **14**, 6526–6532 (2014).
- <sup>38</sup>Y. Zhang, P. Yue, J.-Y. Liu, W. Geng, Y.-T. Bai, and S.-D. Liu, "Ideal magnetic dipole resonances with metal-dielectric-metal hybridized nanodisks," *Opt. Express* **27**, 16143–16155 (2019).
- <sup>39</sup>Z. Wang, Y. Liang, M. Cui, J. Qu, Z. Cheng, and C. Yu, "Bound states in the continuum in plasmonic metasurfaces for enhancing graphene-assisted light modulation," in *TENCON 2022 – 2022 IEEE Region 10 Conference (TENCON)* (IEEE, 2022), pp. 1–3.
- <sup>40</sup>D. Wang, N. K. Emani, T.-F. Chung, L. J. Prokopenko, A. V. Kildishev, V. M. Shalae, Y. P. Chen, and A. Boltasseva, "Plasmon resonance in single- and double-layer CVD graphene nanoribbons," in *2015 Conference on Lasers and Electro-Optics (CLEO)* (IEEE, 2015), pp. 1–2.
- <sup>41</sup>D.-S. Su, D. P. Tsai, T.-J. Yen, and T. Tanaka, "Ultrasensitive and selective gas sensor based on a channel plasmonic structure with an enormous hot spot region," *ACS Sens.* **4**, 2900–2907 (2019).